# Single Free-Falling Droplet of Liquid Metal as a Source of Directional Terahertz Radiation

Petr M. Solyankin,[1,*] Bogdan V. Lakatosh,[2] Mikhail S. Krivokorytov,[2,3] Ilia P. Tsygvintsev,[4]
Anton S. Sinko,[1,5] Igor A. Kotelnikov,[6,7] Vladimir A. Makarov,[5,8] Jean-Louis Coutaz,[9]
Vyacheslav V. Medvedev,[2,3] and Alexander P. Shkurinov[1,5,8,†]

[1] *Institute on Laser and Information Technologies of the Russian Academy of Sciences—Branch of the Federal Scientific Research Center "Crystallography and Photonics" of the Russian Academy of Sciences, Shatura, Moscow Oblast 140700, Russia*

[2] *Moscow Institute of Physics and Technology, Dolgoprudny, Moscow Oblast 141701, Russia*

[3] *Institute for Spectroscopy, Russian Academy of Sciences, Troitsk, Moscow 108840, Russia*

[4] *Keldysh Institute of Applied Mathematics, Russian Academy of Sciences, Moscow 125047, Russia*

[5] *Faculty of Physics and International Laser Center, Lomonosov Moscow State University, Moscow 119991, Russia*

[6] *Budker Institute of Nuclear Physics of the Siberian Branch of the Russian Academy of Sciences, Novosibirsk 630090, Russia*

[7] *Novosibirsk State University, Novosibirsk 630090, Russia*

[8] *The National University of Science and Technology MISiS, Moscow 119049, Russia*

[9] *IMEP-LAHC, UMR CNRS 5130, Universite Savoie Mont-Blanc, Campus Scientifique 73376, Le Bourget du Lac Cedex, France*

We show that an individual droplet of liquid metal can be a source of coherent terahertz radiation when it is excited by two femtosecond laser pulses of the same frequency. Under certain delays between these pulses, the intensity of terahertz radiation increases by more than 3 orders of magnitude. We describe the experimental results with the model of dynamic gain control, which considers the interaction of both laser pulses with the droplet and explains the terahertz-generation process by taking into account the dynamics of electrons and ions after photoionization of the metal droplet. The spatial distribution of terahertz radiation has a forward-directed contribution, whose polarization properties are well described by a nonlinear susceptibility of the second order. Our theoretical estimations based on the experimental data show that under the dynamic gain control the observed terahertz output can be considerably increased. Joint generation of x-ray, ultraviolet, and, as shown in the present work, terahertz radiation allows one to forecast that a free-falling photoexcited droplet of liquid metal is a promising source of multifrequency electromagnetic radiation for extreme nonlinear laser science.

## I. INTRODUCTION

Interaction of intense femtosecond laser pulses with various media is a process commonly used to generate broadband [1,2] and powerful [3] terahertz radiation. It can be used for time-domain spectroscopy [2], terahertz-pump–terahertz-probe experiments [4–6], and even particle acceleration [7,8]. Solid target sources such as nonlinear crystals exhibit material degradation, spectral limitations due to the phonon absorption, and a low damage threshold. Therefore, intense research on gaseous [9], liquid [10], and even-more-complicated clusterized gas sources [11] is conducted.

In our experiment, we use tiny free-falling metallic droplets as a source of terahertz radiation. Such droplets have recently attracted much attention due to the strong extreme UV emission at a wavelength of 13.5 nm under ultrashort optical illumination [12]. Up to 6% conversion efficiency for this phenomenon for specific experimental conditions has been reported [13]. The process of plasma formation from these droplets has been studied in detail for different laser-excitation conditions [14,15].

The possibility to provide fresh solid-density targets for each laser pulse leads to the development of a new type of terahertz source. Previously, terahertz generation was demonstrated on flat [16] and corrugated [17] metallic surfaces, as well as on metal-cluster films [18]. In all these previous studies, the authors had to use moderate optical pulse energies to avoid material damage. The closest

---

*soluankp@yandex.ru

†ashkurinov@physics.msu.ru

experimental analogs of the droplet targets, presented in this paper, are clustered-gas [11,19] and liquid [20,21] jets, where joint generation of terahertz radiation and x-ray radiation was described. Both analogs have locally solid-state density, and under optical excitation can provide dense plasma.

The use of two femtosecond laser pulses delayed in relation to each other [22] or optimization of the laser-pulse duration [23] allows one to increase the efficiency of generation of terahertz radiation due to preliminary ionization of the medium, using nonstationary enhancement of nonlinear response—dynamic gain control. Such studies are known in gases [24], gaseous clusters [22], and very recently in liquids [25,26]. Light-induced enhancement of nonlinear response in the terahertz frequency range was demonstrated for nonlinear metamaterials [27]. In our work, we use free-falling liquid droplets of metal as a medium, where generation of terahertz radiation occurs under a light-induced nonlinear response. A femtosecond laser pulse is absorbed by the droplet, initiating various hydrodynamic and electronic processes occurring on different timescales. The essential factor is the time-dependent dynamics of the temperature of electrons, which indirectly determines the nonlinear response of the medium as well. It is the second laser pulse, delayed in relation to the first one, that generates terahertz radiation, and the optimal time of its delay is determined by electrodynamic parameters of the medium, which is shown in Ref. [23]. When the delay between the two pulses is optimized, enhancement of the generated terahertz power by several orders of magnitude is observed.

## II. EXPERIMENTAL SETUP

Our experimental setup is depicted schematically in Fig. 1. We use a high-temperature dispenser (MJ-SF-01, MicroFab Technologies) with an integrated orifice [28] to create a series of metallic droplets. The droplets fall down due to gravity in a specially designed vacuum chamber with pressure down to $10^{-5}$ mbar. Use of this vacuum chamber prevents droplet oxidation and air breakdown by the femtosecond radiation. More information on the droplet-formation system could be found in Refs. [29,30]. The metal is an eutectic alloy of tin and indium (48% Sn, 52% In), which is in the liquid state due to a preheating process at $140\,°C$. With the help of a piezoelectric actuator bonded to the glass capillary of the dispenser, we are able to synchronize the laser pulses and the appearance of droplets. The droplet size is adjusted by our applying a voltage pulse with an adequate time profile to the actuator. The droplet size and accuracy of the droplet-laser synchronization are controlled by a CCD camera with a resolution of 2.8 $\mu$m per pixel. We use an additional nanosecond-duration backlight laser to see the droplet shape at a
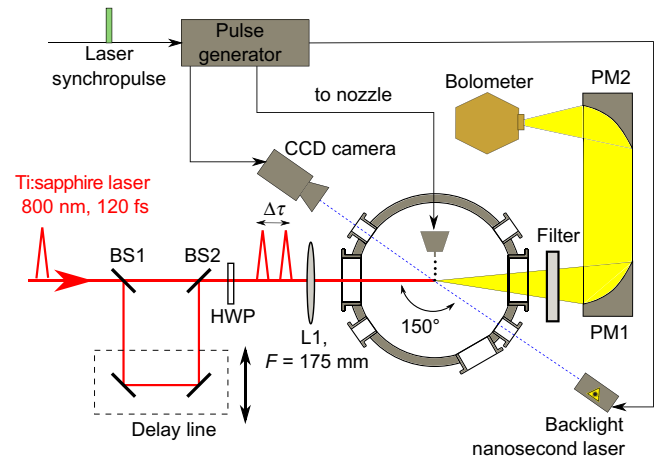


FIG. 1. Experimental setup. BS1, adjustable beam splitter; BS2, 1:1 beam splitter; L1, lens; HWP, half-wave plate; PM1 and PM2, off-axis metallized parabolic mirrors with $F = 150$ mm and an aperture of 50 mm.

variable delay after the arrival of the laser pulse. Characteristic pictures are presented in Fig. 2. The initial droplet is measured to have a characteristic diameter of around 50 $\mu$m with a shape from spherical to slightly elliptical with a ratio of the size in the vertical direction to the diameter in the horizontal plane of up to 1.2.

We use a Spectra Physics Spitfire Ti:sapphire regenerative-amplifier system that delivers optical pump pulses of 120-fs duration, of 800-nm central wavelength, and at a repetition rate of 4 Hz. Such a low repetition rate is chosen
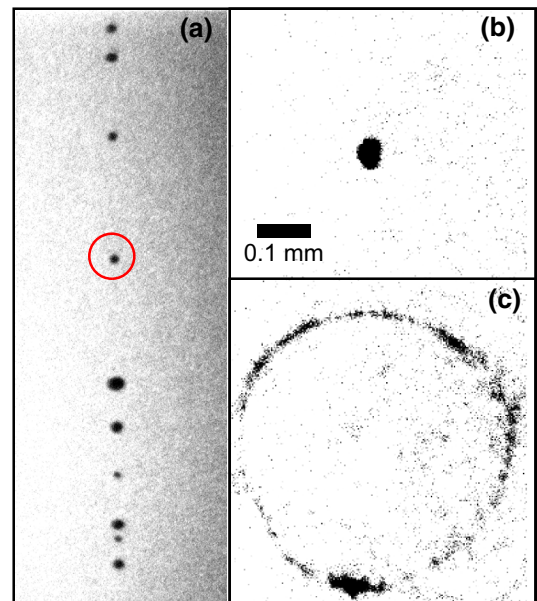


FIG. 2. Droplet shadowgraphs. Droplet sequence with a working droplet (a) and droplet before (b) and 2 $\mu$s after (c) laser-droplet interaction.

to minimize the influence of the droplet fragments on the next droplet and dispenser. The two consecutive copropagating laser pulses that illuminate the sample are produced with use of an adjustable beam splitter (BS1) that can adjust the energy ratio between two pulses, a delay line, and a 1:1 beam splitter (BS2). In this way, the energy of each laser pulse can be varied from 0 to 0.76 mJ with a constant sum energy of 0.76 mJ and we can adjust the delay between the two pulses. The laser beam is focused down to a waist of around 15-$\mu$m FWHM with lens L1 of focal length 175 mm. To finely adjust the position of the focused laser at the center of the droplet, we vary the time delay between the droplet and the laser pulse, which is equivalent to shifting the droplet along the vertical direction, and in the horizontal plane by moving the lens. The main criteria of our adjustments are the symmetry and the velocity of the droplet explosion (see Fig. 2).

Terahertz radiation is generated by the photoexcited droplet. We collect the terahertz radiation behind the droplet along the same axis as the initial laser radiation. This terahertz radiation passes through a 3-mm-thick polypropylene window and additional silicon filters and is focused by two off-axis metalized parabolic mirrors PM1 and PM2, with focal length 150 mm and aperture 50 mm, into a helium-cooled bolometric detector (Infrared Labs). The bolometric detector itself includes low-temperature, low-pass terahertz filters. For most of the experiments, a 3-THz cutoff filter is used. The light-collection angle for our scheme is around 19°. A wire-grid polarizer (Standa Ltd.) is placed between the two parabolic mirrors to select the detected terahertz polarization, and we use a Michelson-type interferometer to measure the terahertz-pulse spectrum. The terahertz detection scheme (PM1, PM2, Bolometer in Fig. 1) is constantly bound to one of the windows of the vacuum chamber.

## III. EXPERIMENTAL RESULTS AND THEIR PHENOMENOLOGICAL EXPLANATION

In our experiments, we do not observe a terahertz signal on excitation of the droplet with only one laser pulse, while an intense signal is observed if the excitation is done by two pulses delayed relative to each other in time. The signal is much stronger in the case when the low-energy pulse hits the droplet before the high-energy pulse. The terahertz signal versus delay between two pulses for a fixed pulse-energy ratio of 39 $\mu$J to 720 $\mu$J is shown in Fig. 3.Both pulses have the same polarization. At positive delays, the pulse with lower energy hits the droplet first. As can be seen in Fig. 3, there is no terahertz emission at zero delay and below. At positive delays, the terahertz signal increases with a characteristic rise time of a few tens of picoseconds, and then after a delay of about 70 ps reaches a plateau, with a slight increase in signal with increasing delay between pulses. The total output energy
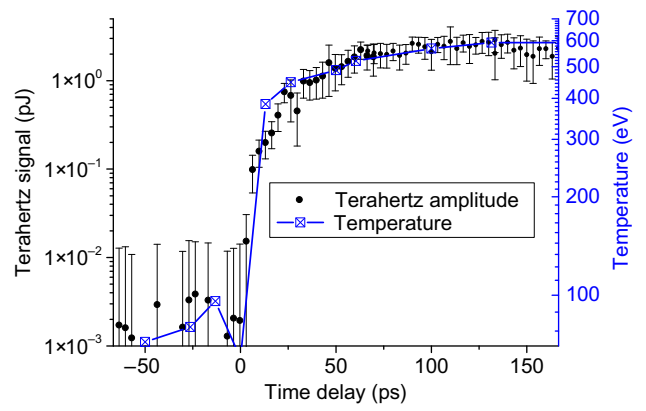


FIG. 3. Amplitude of the terahertz signal for different delays between laser pulses. At positive delays, the low-energy pulse (39 $\mu$J) comes earlier than the second pulse with energy 720 $\mu$J. Black dots represent the experimental data, and blue curves are the results of modeling according to Sec. IV B for the temporal dynamics of the electron temperature on the droplet surface.

at the bolometric detector is about 2 pJ at long delays. We also try the two-color scheme [9], which is frequently used for terahertz generation in air plasma, but do not observe any increase of the signal.

The above-mentioned experimental results clearly demonstrate a significant enhancement of terahertz signal under conditions of plasma formation near and inside the droplet. Under zero delay between the two pulses, which in our model corresponds to one single powerful pulse, the ionization of atoms of metals undoubtedly occurs. However, the ionization itself, as can be seen from our experiment, is not the source of terahertz radiation. Under a positive delay between two pulses, the weak pulse arrives first. It creates the plasma, whose properties change over time. The dynamics of this change are analyzed in Secs. IV A and IV B. With time, the distribution of electrons in the droplet and their temperature change. After some time the parameters of the plasma become optimal for the second pulse, which arrives later, in order to generate terahertz radiation. The fact that the maximum intensity of terahertz radiation appears for quite long delays of the pulse testifies that the source of radiation is not the droplet ionized under the impact of the first laser pulse, but is the result of the longitudinal distribution of electron density under the action of ponderomotive force caused by the second laser pulse. For negative delays (i.e. the powerful pulse comes earlier), for the relation between the pulses described earlier, we observe only a small near noise level signal around −5 ps. The absence of sufficient signal at negative delays is because in this case the energy of the second pulse is not enough for the ponderomotive force caused by it to enhance the terahertz signal. This is shown in additional experiments not presented in this paper where the relation between the pulses changes over a wide range of intensities.
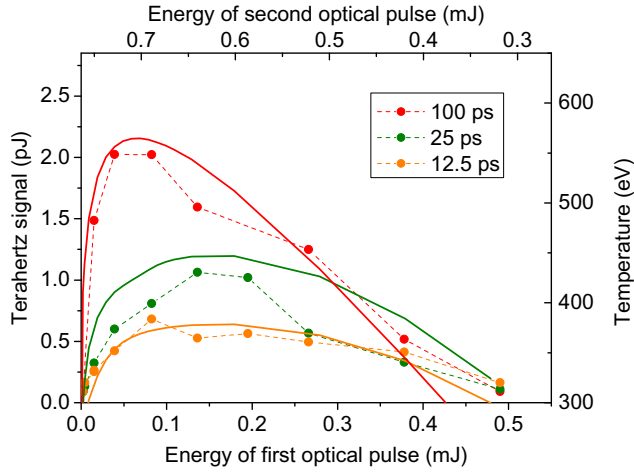
FIG. 4. Dependence of the terahertz-signal intensity of free-falling liquid-metal droplets on the energy of the first and second laser pulses delayed relative to each other. The results are given for three values of relative delays between laser pulses. The plots show experimental results (dashed curves with points) and theoretical calculations (solid curves) by the theoretical approach described in Sec. IV B.

For fixed time delays between pulses there is a wide optimum of the dependence of the terahertz signal on the energy ratio of the two pulses (see Fig. 4). For most delays the position of this optimal point is located near an energy ratio of 100 $\mu$J to 660 $\mu$J.

## A. Polarization of terahertz radiation

Some obtained experimental results can be explained by the slowly-varying-amplitude approach, which was first proposed in Ref. [31]. We assume that a laser pulse with central frequency $\omega$ is linearly polarized in the $x$-$y$ plane. It propagates along the $z$ axis and hits a liquid-metal droplet as shown in Fig. 5. The droplet moves in the gravitational field directed along the $x$ axis. As already mentioned, our droplet could have an elongated form along the $x$ axis with a half-axis ratio of up to 1.2.

As a result of the influence of the first linearly polarized laser pulse on a droplet, its symmetry changes. The latter will be very significant if the angle $\psi$ between the direction of oscillation of its vector of electric field strength and the axis $y$ is small enough. We assume that the final symmetry of the modified droplet is analogous to that of a crystal of the "low category," which has the class of symmetry "1." For this class of symmetry, the quadratic susceptibility tensor has the symmetry by permutation of indices, and its six components are different and differ from zero. Moreover, all 27 components of the tensor of the third rank $\chi_{ijk}^{(2)} = \chi'_{ijk} - i\chi''_{ijk}$, which are not symmetric for the index translation, are also different and are not equal to zero.

If the second femtosecond laser pulse, which propagates along the $z$ axis after the first one, has the same central
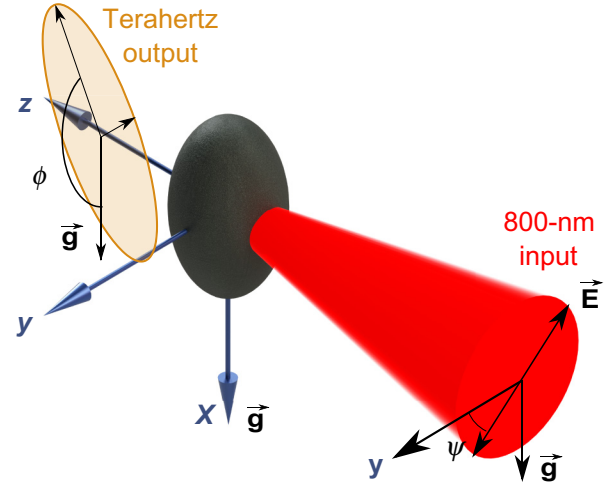


FIG. 5. Angles between the laser beam and the polarization state of the laser pulses and the generated terahertz radiation.

frequency $\omega$ and amplitude $E_0$, difference-frequency generation leads to the occurrence of terahertz radiation with frequency $\Omega$ due to the interaction of its spectral components with frequencies $\Omega + \omega/2$ and $\omega - \Omega/2$.

The equations for the Cartesian components of the electric-field-strength vector of the generated terahertz radiation are

$$\frac{\partial^2 E_x}{\partial z^2} + \frac{\Omega^2}{c^2}\varepsilon_{xx}E_x + \frac{\Omega^2}{c^2}\varepsilon_{xy}E_y = -\frac{4\pi\Omega^2}{c^2}P_x, \quad (1)$$

$$\frac{\partial^2 E_y}{\partial z^2} + \frac{\Omega^2}{c^2}\varepsilon_{yy}E_y + \frac{\Omega^2}{c^2}\varepsilon_{yx}E_x = -\frac{4\pi\Omega^2}{c^2}P_y, \quad (2)$$

where $P_x$ and $P_y$ are the components of the complex vector amplitude of the quadratic polarization of the medium at the terahertz frequency induced by the second pulse. Let us assume that $\text{Re}\,\varepsilon_{xx} = \varepsilon + \Delta$ and $\text{Re}\,\varepsilon_{yy} = \varepsilon - \Delta$, where $\text{Re}\,\varepsilon_{xy} \approx \Delta \ll \varepsilon$ (see Sec. IV). We want to find a solution to Eqs. (1) and (2) using the slowly-varying-amplitude method in the form $E_x = A_x(z)\exp(-ikz)$ and $E_y = A_y(z)\exp(-ikz)$, where $k = \Omega\sqrt{\varepsilon}/c$. The complex amplitude $A_x(z)$ or $A_y(z)$ is a solution of the system of nonhomogeneous linear differential equations

$$\frac{\partial A_x}{\partial z} + i\frac{\Omega\Delta}{2c\sqrt{\varepsilon}}A_x + i\frac{\Omega\varepsilon_{xy}}{2c\sqrt{\varepsilon}}A_y + \delta_x A_x$$
$$= -i\frac{2\pi\Omega}{c\sqrt{\varepsilon}}P_x\exp(i\Delta kz), \quad (3)$$

$$\frac{\partial A_y}{\partial z} - i\frac{\Omega\Delta}{2c\sqrt{\varepsilon}}A_y + i\frac{\Omega\varepsilon_{yx}}{2c\sqrt{\varepsilon}}A_x + \delta_y A_y$$
$$= -i\frac{2\pi\Omega}{c\sqrt{\varepsilon}}P_y\exp(i\Delta kz), \quad (4)$$

which satisfy the boundary condition $A_x(0) = A_y(0) = 0$. In Eqs. (3) and (4) $\Delta k$ is the phase mismatching of the wave vectors and $\delta_x$ and $\delta_y$ are the linear absorption coefficients. Since the droplet size is small, we present approximated solutions of Eqs. (3) and (4) as a Taylor expansion in a series of "$z$" with accuracy to linear terms:

$$E_x \approx -i\frac{2\pi\Omega}{c\sqrt{\varepsilon}}P_x z,$$
$$E_y \approx -i\frac{2\pi\Omega}{c\sqrt{\varepsilon}}P_y z. \tag{5}$$

We measure the ellipticity of the polarization ellipse $M(\psi) = (|E_+|^2 - |E_-|^2)/(|E_+|^2 + |E_-|^2)$, where $E_\pm = E_x \pm iE_y$ and $\Phi(\psi) = \arg(E_- E_-^*/2)$ is the rotation angle of the main axis of the terahertz-radiation-polarization ellipse. The rotation angle depends on the intensity of the laser field and is measured in relation to the direction of the $x$ axis, and can be found from Eq. (5). When the oscillations of the electric field vector in both femtosecond pulses occur along the $y$ axis ($\psi = 0°$), the components $P_x$ and $P_y$ are given by

$$P_x \approx (\chi'_{xyy} - i\chi''_{xyy})E_0^2, \tag{6}$$

$$P_y \approx (\chi'_{yyy} - i\chi''_{yyy})E_0^2, \tag{7}$$

and accurate to the approximations made we obtain

$$M(\psi = 0) = \frac{2(\chi'_{xyy}\chi''_{yyy} - \chi''_{xyy}\chi'_{yyy})}{\chi'^2_{yyy} + \chi''^2_{yyy} + \chi'^2_{xyy} + \chi''^2_{xyy}}, \tag{8}$$

$$\Phi(\psi = 0) = \frac{1}{2}\arctan\left(\frac{2(\chi'_{xyy}\chi'_{yyy} + \chi''_{xyy}\chi''_{yyy})}{\chi'^2_{yyy} + \chi''^2_{yyy} - \chi'^2_{xyy} - \chi''^2_{xyy}}\right). \tag{9}$$

If the oscillations of the electric field vectors of both pulses occur along the $x$ axis ($\psi = 90$), then an $x$-$z$ symmetry plane arises in the problem, which leads to certain relations between the components of tensor $\chi^{(2)}_{ijk} = \chi'_{ijk} - i\chi''_{ijk}$ and the equality of some of them to zero. In this case $P_x \approx (\chi'_{xxx} - i\chi''_{xxx})E_0^2$, but $P_y = 0$. Both the ellipticity $M(\psi = 90°)$ and the intensity-dependent angle of rotation of the main axes of the polarization ellipse $\Phi(\psi = 90°)$ are zero in this case.

The ratio of the minor and major axes of the polarization ellipse $\epsilon_{ab}$ is related to the ellipticity $M$ of the polarization ellipse by the simple relation

$$\epsilon_{ab} = \frac{1 - \sqrt{1 - M^2}}{1 + \sqrt{1 - M^2}}.$$

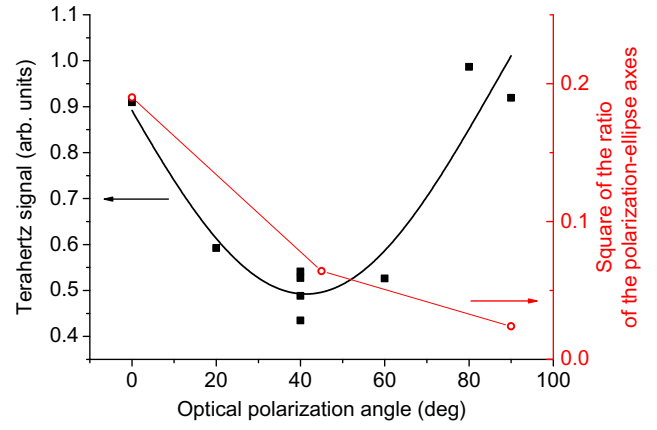We measure some polarization properties of our signal.



FIG. 6.  Total terahertz power (black squares) and $\epsilon_{ab}^2 = b^2/a^2$ (red circles) versus the laser polarization angle $\psi$, where $a$ and $b$ are the major and minor axes of the polarization ellipse. Zero corresponds to horizontal polarization of optical pulses.

We work at a fixed delay of 166 ps and energy ratio of 39 $\mu$J to 720 $\mu$J. The change of the polarization direction for the first, weak pulse does not lead to a change in the total energy or polarization state of the terahertz radiation. We observe that the polarization direction of the terahertz radiation is the same as the polarization direction of the high-energy pulse, but surprisingly, the total energy and ellipticity also depends on it. This is illustrated in Figs. 6 and 7. The convergence of $M(\psi)$ to zero when $\psi$ approaches 90° is confirmed by our experiment (see Fig. 6). When $\epsilon_{ab}$ is on the order of 0.02, the ratio of the lengths of the minor and major axes of the polarization ellipse become on the order of 0.1 (i.e., the difference between polarization of the measured terahertz signal and the ideal linear polarization is less than 10%). This is
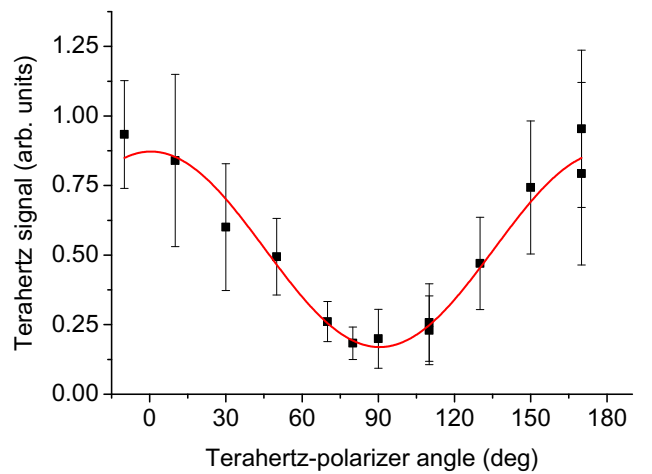


FIG. 7.  Terahertz power versus the angle of the terahertz-polarizer rotation. Dots corresponds to the experimental data and the red line is a sine fit. Zero corresponds to horizontal polarization. The optical polarization for both pulses is horizontal.

already achieved at $M < 0.3$. It is necessary to emphasize that for $M < 0.1$, this difference is already less than 0.25%. The slight difference of $\epsilon_{ab}$ from zero at $\psi = 90°$ in our experiment is due to the approximations which we made when solving the system of equations (3) and (4), polarization-measurement errors, and the residual amount of noncoherent radiation.

## B. Spectrum of terahertz radiation

The spectrum of the emitted radiation is presented in Fig. 8. We measure the spectrum at the same delay of 166 ps and with the same pulse energies by polarization measurements. Because of the moderate signal-to-noise ratio, Fig. 8 is plotted on a linear scale for the spectral energy axis, while usually its scale is logarithmic. To increase the signal-to-noise ratio, we average 100 realizations of interferogramms from the Michelson-type interferometer and then perform a Fourier transform to get the spectrum. The central frequency is about 1.15 THz with a FWHM of 1.5 THz. The polymer-output-window absorption rises with the increase of the terahertz frequency [32], which occurs for terahertz frequencies above 2.5 THz. Nevertheless, it clearly shows that droplet's terahertz-emission spectrum is located at lower frequencies than in the case of a two-color air-based source. However, for a one-color optically induced plasma in air [33], the peak of the spectrum is also located near or even lower than 1 THz. If we use the electron-plasma-frequency approach [1] we can conclude that the most-active region of terahertz emission has lower electron density $n_e$ than in the case of air-based plasma. However, from Fig. 10 it is clear that the near-droplet area has huge gradients for all parameters at near-wavelength sizes even for optical radiation, so this approach is not applicable.
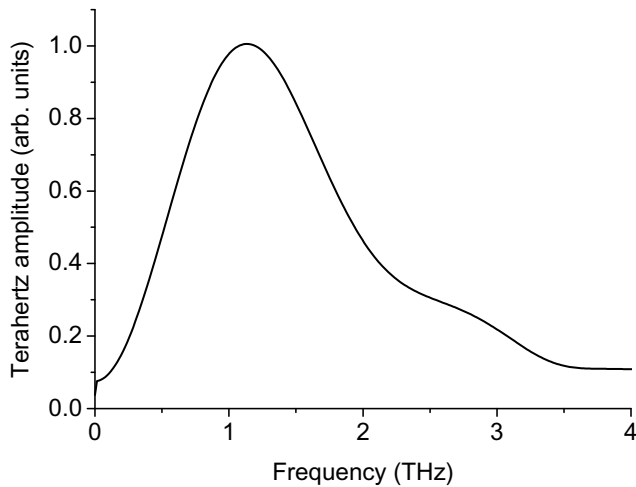


FIG. 8. Spectrum of the emitted radiation. The curve is measured at a delay of 166 ps.

## IV. EXPERIMENTAL RESULTS IN THE FRAME OF SOME THEORETICAL MODELS

### A. Ionization of the droplet by the laser pulse

Hereinafter, we treat the case of creation of a plasma at the droplet surface by the first impinging laser pulse, and the generation of terahertz waves from the excitation of this plasma by the second laser pulse. Some simplification hypotheses are valid.

First, the laser spot size (approximately 15 $\mu$m) is smaller than the droplet size (approximately 50 $\mu$m), and during the typical delays between two pulses of hundreds of picoseconds, the droplet-shape transformation can be ignored [34]. Moreover, the droplet movement during laser excitation is also negligible, and thus the droplet can be considered as being immobile. In the experiment, the total laser energy is divided between two pulses as 39 $\mu$J and 720 $\mu$J. We can then estimate the laser intensity for the low-energy pulse $S_1$ to be $2 \times 10^{14}$ W/cm$^2$, which creates the plasma, and the laser intensity for the high-energy pulse $S_2$ to be $3 \times 10^{15}$ W/cm$^2$. The electric field in the focal spot of the first pulse is on the order of 0.5 GV/cm and approaches one tenth of the characteristic atomic field as given by the Bohr model for hydrogen, $E_a = 5.14$ GV/cm.

According to Refs. [35,36], at such intensities about 20%–25% of light is absorbed for the case of a flat surface. This prediction is in agreement with the results of measuring the complex refractive index of tin. According to the data in Ref. [58], at the wavelength $\lambda = 800$ nm the complex refractive index is given by $\sqrt{\varepsilon} = 2.38 + 6.68i$. The coefficient of reflection of the laser radiation can be calculated by the formula

$$R = \left| \frac{1 - \sqrt{\varepsilon}}{1 + \sqrt{\varepsilon}} \right|^2. \tag{10}$$

For the alloy of 48% Sn and 52% In, the reflection coefficient $R \approx 0.85$ (i.e., about 15% of laser radiation is absorbed within the liquid-droplet thin skin layer). Use of Eq. (10) is still possible with the spherical droplet, as the laser beam hits it at its center, where the spherical surface is almost flat. The skin layer thickness is evaluated by the formula

$$\delta = 1/\text{Im}(\omega\sqrt{\varepsilon}/c). \tag{11}$$

With the refractive index of Sn given above, this yields $\delta = 19$ nm.

Knowing that the concentration of atoms $n_a$ in liquid Sn-In alloy is approximately $3.5 \times 10^{22}$ cm$^{-3}$ and $\xi \approx 15\%$ of the laser-pulse energy is absorbed in the skin layer of thickness $\delta \approx 20$ nm, we can easily calculate the energy

absorbed per atom of the alloy:

$$W_1 = \frac{\xi S \tau}{\delta n_a} \approx 400 \text{ eV},$$ (12)

where the pulse duration $\tau = 120$ fs and the laser power density is $2 \times 10^{14}$ W/cm$^2$.

Another characteristic quantity that will be useful for the analysis of the plasma properties is the energy of the electron quiver oscillations in the laser field in a collisionless approximation:

$$W_e = \frac{m_e}{2} \left( \frac{eE_\omega}{m_e\omega} \right)^2,$$

where $e$ and $m_e$ are the charge of an electron and its mass, respectively. For the field strength $E_\omega = 0.5$ GV/cm estimated in the focal spot, $W_e \approx 20$ eV. This estimation does not take into account that the field in the plasma is different from the field in a vacuum. Under normal incidence, the electric field inside the plasma $E_{\text{in}} = 2E/ \left( 1 + \sqrt{\varepsilon} \right)$. Therefore, the quiver energy is given by $W_e \approx 1.6$ eV. We may use the Drude-model permittivity for $\varepsilon$,

$$\varepsilon = 1 - \frac{\omega_p^2}{\omega \left( \omega + i\nu_{ei} \right)},$$ (13)

to evaluate the plasma frequency $\omega_p$ and the frequency of electron-ion collision $\nu_{ei}$ from the value of the complex permittivity given above. We get $\omega_p = 1.90 \times 10^{16}$ s$^{-1}$ and $\nu_{ei} = 1.87 \times 10^{15}$ s$^{-1}$. Note that the plasma-frequency magnitude found in this way is approximately 2 times higher than the value calculated in accordance with its definition,

$$\omega_p = \sqrt{4\pi e^2 n_e/m_e},$$ (14)

under the assumption that the concentration of free electrons is equal to the concentration of atoms (i.e., $n_e = n_a$). Also note that the calculated collision frequency is slightly less than the circular frequency of the laser pulse $\omega = 2.35 \times 10^{15}$ s$^{-1}$. Below we use a similar approach to estimate other parameters by evaluating the quantities in different ways. For example, we do not know reliably the energy of free electrons torn from atoms during ionization; therefore, we estimate a plausible range of values for the electron mean energies.

The laser-pulse energy absorbed in the skin layer is expended on the evaporation of the melt and subsequent ionization of the vapor. Let us assume that the atoms in the metal droplets are ionized, and each of them supplies the free-electron gas of the alloy with one $5p$ electron. The energy per atom needed for the evaporation of liquid tin $J_0 = 3.07$ eV. The ionization potentials $J_Z = J_1, J_2, \ldots J_{10}$ of the first ten electrons are found in Ref. [37].

The sum of the energies from $J_0$ to $J_7$ is 412 eV. This is comparable in magnitude to $W_1$. Consequently, it can be expected that the energy of the laser pulse is sufficient for the ionization of not more than seven electrons per atom. Actually, the ionization state is expected to be lower than VII because of energy losses through various additional channels.

Primary ionization of tin atoms is done by the strong electric field of the laser pulse. It is necessary to distinguish between barrier-suppression (over-barrier), tunnel, and multiphoton ionization. The strongest electric field is required for over-barrier ionization. Such ionization is possible if the electric field strength exceeds the critical value [19]:

$$E_{\text{cr}} = \frac{Z^3}{16} E_a.$$ (15)

Comparing the values given by Eq. (15) for different charges $Z$ of the ionic residue with $E_\omega \approx 0.5$ GV/cm, we conclude that barrier-suppression ionization is possible for one or two external valence electrons. However, tunneling and multiphoton ionization could occur simultaneously with the barrier-suppression process. These two types of ionization differ in the value of the Keldysh parameter:

$$\gamma_n = \frac{\sqrt{2m_e J_n}}{eE_\omega} \omega.$$ (16)

Tunnel ionization corresponds to $\gamma_n \ll 1$, while multiphoton ionization is characterized by $\gamma_n \gg 1$. The probability of ionization per unit time by an alternating field (Keldysh problem) is determined as the solution of problem 3 in Sec. 77 of *Quantum Mechanics* by Landau and Lifshitz [38]:

$$w_n \sim \omega_a \exp\left[ -\frac{2J_n}{\hbar\omega} f\left(\gamma_n\right) \right],$$ (17)

where

$$f\left(\gamma_n\right) = \left(1 + \frac{1}{2\gamma_n^2}\right) \text{arcsinh } \gamma_n - \frac{\sqrt{1 + \gamma_n^2}}{2\gamma_n}$$ (18)

and $\omega_a = m_e e^4/\hbar^3 \approx 4 \times 10^{16}$ s$^{-1}$ is the atomic unit of frequency. Using these formulas and $J_1 = 7.34$ eV, $J_2 = 14.63$ eV, and $J_3 = 30.52$ eV, we find

$$\tau_1 = 1/w_1 = 1.92 \times 10^{-3} \text{ fs},$$

$$\tau_2 = 1/w_2 = 3.40 \text{ fs},$$

$$\tau_3 = 1/w_3 = 8.13 \text{ ms}.$$

Consequently, the first electron escapes from the tin or indium atom in about one period of the laser-pulse field. It takes several femtoseconds to tear out the second electron, and tearing out the third electron by the laser field is

almost impossible. However, the first torn-out electron, as we have seen, acquires an energy on the order of $W_1$, which is obviously sufficient for secondary ionization by electron impact.

To estimate the cross section of ionization by electron impact, we use the Thomson formula [39]:

$$\sigma_{\text{II}} = 4\pi a_B \frac{J}{\epsilon} \left(1 - \frac{J}{\epsilon}\right), \qquad (19)$$

where the subscript II means "impact ionization," $J$ is the ionization potential, and $\epsilon$ is the electron energy. The ionization time is calculated by the formula

$$\tau_{\text{II}} = \frac{1}{n_e \sigma_{\text{II}} v_e}, \qquad (20)$$

where $v_e = \sqrt{2\epsilon/m_e}$. For $\epsilon = W_1$ and $J = J_1$ we get $\tau_{\text{II}} \approx$ 4 fs. The time of the reverse process of triple recombination is estimated by the formula [40]

$$\tau_{\text{IR}} = \frac{(T_e/J)^2}{64\pi^2 \alpha c a_B^5 n_e n_i}, \qquad (21)$$

where the subscript IR means "impact recombination," $\alpha$ is the fine-structure constant, $a_B$ the Bohr radius, $T_e$ and $n_e$ are the electron temperature and density, respectively, and $n_i$ is the ion density. For $T_e = W_1$, $J = J_1$, and $n_e = n_i = n_a$, we get $\tau_{\text{IR}} \approx 4$ ps. Estimating the time of photorecombination by the formula [41]

$$\tau_{\text{RR}} = \frac{(T_e/J_Z)^{1/2} + 0.652(T_e/J_Z) + 0.214(T_e/J_Z)^{3/2}}{8.41\left[\ln\left(1 + J_Z/T_e\right) + 3.50\right]\alpha^4 c Z a_B^2 n_i}, \qquad (22)$$

where the subscript RR means for "radiative recombination," we get $\tau_{\text{RR}} = 0.4\ \mu$s.

We see that radiative recombination is too slow, but triple recombination can occur in the interval between successive laser pulses (this interval is about 10–20 ps). Therefore, it can be expected that ionization equilibrium is established in the ionized layer as suggested in Ref. [42]. The slowness of radiation recombination also means that the recombination radiation is weak. As stated in Ref. [43], only 0.3% of the energy of the laser pulse goes into x-ray radiation.

As noted above, the energy $W_e$ related to electron oscillation induced by the laser field is many times less than the energy $W_1$ that is absorbed by an individual atom in the skin layer. We try to find out whether a free electron has time to accelerate to energy $W_1$ as a result of Coulomb collisions.

The frequency of electron-ion collisions can be estimated by the formula [44]

$$\nu_{ei} = 3.9 \times 10^{-6} \Lambda Z^2 n_i \epsilon^{-3/2}\ (\text{eV}^{3/2}\ \text{cm}^3/\text{s}), \qquad (23)$$

where $\Lambda = 15$ is the Coulomb logarithm. For $Z = 1$, $n_i = n_a$, and electrons with energy $\epsilon = W_1$, we have $\nu_{ei} \approx 3 \times 10^{14}\ \text{s}^{-1}$, which is more than 1 order of magnitude lower than the value $1.87 \times 10^{15}\ \text{s}^{-1}$ obtained with the Drude model. The corresponding time of electron-ion collisions is

$$\tau_{ei} = 1/\nu_{ei} \approx 4\ \text{fs}. \qquad (24)$$

As the degree of ionization increases, the collision frequency increases (i) in proportion to the square of the average ion charge $Z^2$ and (ii) in proportion to $Z^{3/2}$ because of the decrease in the average electron energy $\epsilon \approx W_1/Z$ (if we ignore the energy costs of ionization); therefore, $\tau_{ei} \propto Z^{-7/2}$.

The frequency of electron-electron collisions is estimated with the following formula [44]:

$$\nu_{ee} = 7.7 \times 10^{-6} \Lambda n_e \epsilon^{-3/2}\ (\text{eV}^{3/2}\ \text{cm}^3/\text{s}). \qquad (25)$$

For $Z = 1$, $n_e = n_a$, and $\epsilon = W_1$, it yields $\nu_{ee} \approx 3 \times 10^{14}\ \text{s}^{-1}$, so the Maxwellization time of the electron distribution is $\tau_{ee} = 1/\nu_{ee} \approx 2$ fs. As the average ion charge increases, the time of electron-electron collisions changes according to the law $\tau_{ee} \propto Z^{-5/2}$.

The heating of ions by electrons is characterized by the ion-electron collision time, which is approximately $M/m_e$ times greater than $\tau_{ei}$ ($M$ is the mass of the ions) [45]:

$$\tau_{ie} = (M/m_e)\, \tau_{ei} \approx 0.2\ \text{ps} \qquad (26)$$

with $\epsilon = W_e$ and

$$\tau_{ie} = (M/m_e)\, \tau_{ei} \approx 800\ \text{ps} \qquad (27)$$

with $\epsilon = W_1$. For a lower energy such as $\epsilon \sim W_e$ the thermalization time $\tau_{ie}$ is much shorter. Therefore, by the time of the arrival of the second pulse, the temperatures of the electrons and ions can become equal if the temperature of the electrons drops due to the energy expended on ionization.

Summarizing the above assessments, we can assume that, in the expanding ablation layer, at the time the second laser pulse arrives (i.e., after 10–20 ps), the ionization equilibrium is established. The temperatures of electrons and ions become approximately equal, and the thermal energy per electron or per ion of the plasma drops to units or even fractions of an electronvolt. The second laser pulse excites forced oscillations in the resulting plasma with a characteristic frequency inverse to the pulse duration. These oscillations give rise to terahertz radiation.

### B. Material motion and droplet emission

To estimate the effect of the first pulse on the droplet temperature, we perform a series of hydrodynamic simulations in the one-fluid, two-temperature approximation. The qualitative dynamics of the laser-pulse interaction with droplet is presented in Fig. 9.According to the time separation, we can single out three stages of laser-droplet interaction:

(a)  First, the interaction of the femtosecond laser pulse with electrons of the target occurs on the femtosecond timescale. The characteristic features of this timescale are the barrier-suppression mechanism of ionization, the non-Maxwellian distribution of electrons, etc. The suggested theoretical model is not formally applicable on this timescale because it does not take into account all these factors. However, when the pulse is over, the electron distribution becomes Maxwellian on the femtosecond timescale, and finally all these complex processes result in some distribution of electron temperature and density in the surface layer of the droplet. Using the experimental values for the skin layer and the reflection coefficient, we avoid a direct simulation of this early femtosecond stage, expanding the range of applicability of our model.

(b)  Then, the interaction between ions and electrons occurs on the picosecond timescale: relaxation of electron and ion temperature, establishment of stationary ionization by collision mechanism, etc. A two-temperature approach is applicable at this stage, but we make two simplifications in our model. Firstly, we use coefficients, derived for an ideal plasma, which allow us to estimate only the order of magnitude for the time of temperature-equilibrium establishment. Secondly, we ignore the dynamics of ionization, assuming that the electron and ion density are related as $n_e = n_i Z_i(\rho, T_e)$. However, insofar as motion at this stage is negligible, and final equilibrium of ion and electron subsystems is described properly, the related integral error should also be low. From comparison of collisional ionization rates with the time of hydrodynamic expansion, we estimate this error is less than 20%.

(c)  The timescale of tens of picoseconds is characterized by the motion of the plasma. As the energy input is quite small, we can ignore the spatial separation of ions and electrons and apply a one-fluid hydrodynamics approach. Errors from the previous stages can result in the wrong degree of ionization and electron temperature, which means inaccurate pressure values. Thus, we can expect qualitatively correct dynamics by applying our model for the whole process on a timescale of tens of picoseconds, with possible error in the resulting plasma-expansion velocity $u$.

With the energy of the laser pulses used in our experiment and the delay times between them, the thickness of the plasma layer at the droplet surface does not exceed approximately 5 $\mu$m (see Fig. 10 for a typical plasma distribution). This value is much less than the diameter of the droplet of approximately 50 $\mu$m and the laser-beam diameter at the droplet surface of 15 $\mu$m. This allows us to implement a one-dimensional approach in the analysis of the plasma dynamics. We assume that laser radiation
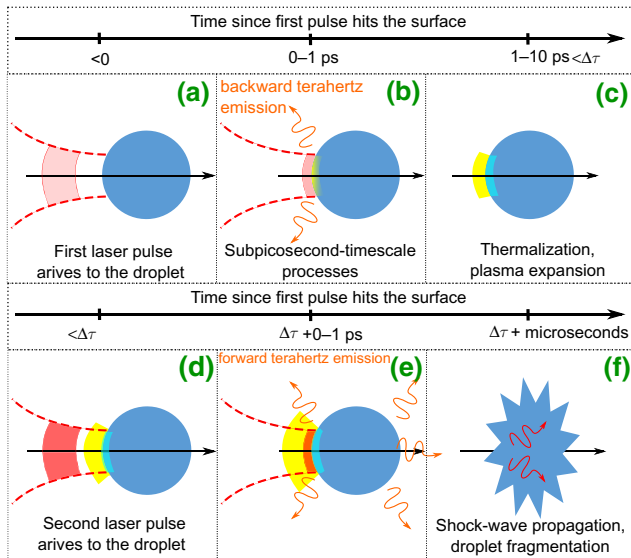


FIG. 9.   Different stages of the interaction of femtosecond radiation with a droplet and terahertz-radiation emission.
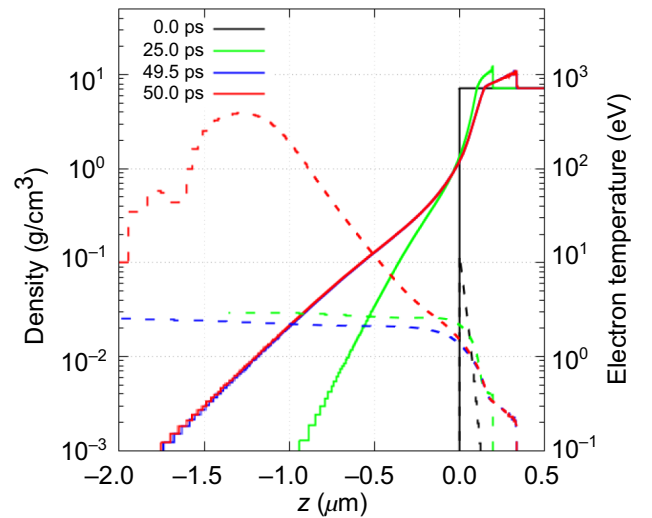


FIG. 10.   Simulated dynamics of density and electron temperature for the first pulse (energy 39 $\mu$J), the second pulse (energy 720 $\mu$J), and delay between them (50 ps). Presented are distributions at the start of the simulations, in the middle of the delay, just before the second pulse, and at the peak of the second pulse. Solid lines are densities, and dashed lines temperatures. THe position of the shock wave can be determined from the small step in the density distribution in the $z > 0$ region.

is absorbed by the electron subsystem. On one hand, the laser-pulse duration is much shorter than the time for equilibration of the electron and ion temperatures. On the other hand, it is much longer than the time for electron thermalization. For these reasons, we need to apply a two-temperature model for the simulation. As the energy input is quite small, we can ignore the spatial separation of ions and electrons. Therefore, the one-dimensional one-fluid hydrodynamic system is governed by the following thermal conditions and radiation-transfer equations (continuity equation, Euler equation, and energy equation [46]):

$$\frac{d\rho}{dt} = -\rho \frac{\partial v}{\partial z},$$

$$\rho \frac{dv}{dt} = -\frac{\partial}{\partial z}(P_e + P_i),$$

$$\frac{d\varepsilon_e}{dt} = -P_e \frac{d(1/\rho)}{dt} + \frac{1}{\rho}\frac{\partial}{\partial z}\kappa_e \frac{\partial T_e}{\partial z} + Q_{ei} + G_e^{\text{rad}} + G_e^{\text{las}},$$

$$\frac{d\varepsilon_i}{dt} = -P_i \frac{d(1/\rho)}{dt} + \frac{1}{\rho}\frac{\partial}{\partial z}\kappa_i \frac{\partial T_i}{\partial z} - Q_{ei},$$

(28)

where $t$ is the time, $z$ is the coordinate normal to the droplet surface (laser pulse is going from $z = -\infty$), $d/dt = \partial/\partial t + v\,\partial/\partial z$ is the substantial time derivative, $\rho$ is the density, $v$ is the $z$ component of the velocity, $T_e$, $P_e$, and $\varepsilon_e$ are the temperature, partial pressure, and specific internal energy of electrons, respectively, $T_i$, $P_i$, and $\varepsilon_i$ are the temperature, partial pressure, and specific internal energy of ions, respectively, $\kappa_e$ and $\kappa_i$ are the electron thermal conductivity and the ion thermal conductivity, respectively, $Q_{ei}$ is the heat exchange between electrons and ions, $G_e^{\text{las}}$ is the laser energy deposited, and $G_e^{\text{rad}}$ is the energy transferred due to absorption and emission of thermal radiation.

For the ion subsystem, the ideal-gas equation of state is used. The equation of state of electrons as well as the degree of equilibrium ionization are calculated with the Thomas-Fermi model with half-empirical corrections [47] (FEOS code, [48]). For the ion thermal conductivity and $Q_{ei}$, Braginsky's expressions for an ideal plasma are used [49], and the electronic thermal conduction is modeled with a semiempirical formula [50] based on the Spitzer expression [51]. Thermal radiation transport is calculated by the multigroup-diffusion approximation. Averaged over spectral groups, opacities and emissivities as functions of temperature and density are calculated with the THERMOS code [52].

The absorption of the first pulse is resolved in time: instead the energy absorbed into the skin layer is described by an exponential law, assuming the heating is proportional to the square of the field and ignoring heat transfer during the first pulse. The coefficient of absorption and the layer thickness are determined from the experimental data, as described in Sec. IV A. The resulting distribution of the electron energy density is used to calculate the initial distribution of the electron temperature (see Fig. 10, dashed black line).

Absorption of the second laser pulse is calculated by our using the one-dimensional Helmholtz equation [53], assuming inverse bremsstrahlung as the main absorption process [50].

To solve numerically the system of equations (28) we use a second-order fully conservative finite-difference scheme with a staggered grid. Typical results of the simulation are presented in Fig. 10. Parameters of matter are depicted as piecewise constant functions with a step, defined by the numerical mesh resolution.

Th initial distribution is the solid-state density and electron temperature, exponentially decreasing with distance from the surface. Assuming absorption of 15% for the 39-$\mu$J first pulse, we get absorption of 1.7 J/cm$^2$ in the 20 nm layer, leading to a temperature of approximately 12 eV (or approximately $1.3 \times 10^4$ K) at the surface, which is much higher than the thresholds of evaporation and ionization for tin. Such an overheated layer causes rapid expansion of the ionized matter outside the surface (exponentially increasing density profiles at $z < 0$ in Fig. 10) and a shock wave propagating inside the droplet (steps at $z = 0.2$ and 0.3 $\mu$m). While the temperature in the expanding plasma decreases due to radiation emission and conversion to kinetic energy, the velocity increases. As we see from the results of our simulations, the resulting complex dynamics of the plasma density at large distances from the surface is well described with an automodel solution:

$$\rho(z, t) \approx \rho_0 \exp\left(\frac{z}{ut}\right),$$

(29)

where $\rho_0$ is a constant and $u$ is the constant velocity of expansion.

With this observation, the resulting dependence of the maximum temperature on the delay time $\Delta t$ between pulses can be qualitatively explained. We assume that the temperature $T_e$ and the ionization degree $Z_i$ of the plasma are constants in space and time in the region where Eq. (29) is valid (region $z < -0.2$ $\mu$m in Fig. 10). Then the electron density is strictly proportional to $\rho$, and at $\Delta t$ is given by

$$n_e(z) \approx n_e^0 \exp\left(\frac{z}{u\Delta t}\right).$$

(30)

The refractive index of an ideal plasma $n = \sqrt{1 - n_e^2/n_c^2}$, where $n_c \sim \lambda^{-2}$ is the critical electron density. For the wavelength of 0.8 $\mu$m considered, the value is $1.7 \times 10^{21}$ cm$^{-3}$. In the region $n_e > n_c$, the refractive index becomes imaginary, and thus the electromagnetic field is exponentially decreasing. Assuming that all the laser-pulse energy is absorbed in the region $n_e \ll n_c$, we can estimate the laser heating with the following consideration.

The absorption coefficient due to inverse bremsstrahlung is given by $\kappa \sim n_e n_i Z_I^2$ and its spatial dependence is given by

$$\kappa(z) \approx \kappa_0 \exp\left(\frac{2z}{u\Delta t}\right). \qquad (31)$$

Assuming that $S_0$ is the laser-flux density of the second pulse near the droplet but outside the plasma, the laser flux at finite distance $z$ inside the plasma is given by

$$S(z) = S_0 \exp\left[-\int_{-\infty}^{z} \kappa(z')dz'\right]$$
$$\approx S_0 \exp\left[-\frac{\kappa_0 u\Delta t}{2} \exp\left(\frac{2z}{u\Delta t}\right)\right]. \qquad (32)$$

The resulting laser energy absorbed per unit volume is then givne by

$$\Delta E_e(z) = -\frac{\partial S}{\partial z} \approx S_0 \kappa_0 \exp\left[\frac{2z}{u\Delta t} - \frac{\kappa_0 u\Delta t}{2} \exp\left(\frac{2z}{u\Delta t}\right)\right]. \qquad (33)$$

Assuming we can still use the ideal-gas expression $\Delta E_e = 3/2 \times n_e k \Delta T_e$ to relate electron energy density and temperature, we obtain the temperature rise produced by the second pulse as

$$k\Delta T_e(z) \approx \frac{2}{3} \frac{S_0 \kappa_0}{n_e^0} \exp\left[\frac{z}{u\Delta t} - \frac{\kappa_0 u\Delta t}{2} \exp\left(\frac{2z}{u\Delta t}\right)\right]. \qquad (34)$$

Its maximum value is given by

$$k\Delta T_e^{\max} = \frac{2}{3e} \frac{S_0}{\sqrt{u\Delta t}} \frac{\sqrt{\kappa_0}}{n_e^0}. \qquad (35)$$

This consideration completely ignores reflection, assuming that only a small part of the laser light reaches the critical surface. So its applicability is restricted by the condition $S(z_c) \ll S_0$, where $z_c = -u\Delta t \ln(n_e^0/n_c)$ is the position of the critical surface $n_e = n_c$ at the moment $\Delta t$. After some calculations, we get the condition that must fulfill the minimum delay:

$$u\Delta t \gtrsim \frac{2}{\kappa_0}\left(\frac{n_e^0}{n_c}\right)^2. \qquad (36)$$

When this condition is fulfilled, the maximum temperature should follow Eq. (35) and decrease as $\Delta t^{-0.5}$. On the other hand, when the plasma layer is not thick enough to effectively screen the metal, a significant part of the laser energy is reflected, and the rest is absorbed in the region $n_e \gg n_c$, leading to lower $T_e^{\max}$ at lower delays. Since $u \sim E_1^{\alpha}$, where

$0 < \alpha < 1$, for every fixed value of the first-pulse energy $E_1$, there should be a value of the delay providing the maximum temperature, and this optimal delay is lesser for higher $E_1$.

### C. Angular distribution of terahertz-radiation emission

As demonstrated by the numerical simulation shown in Fig. 10, the first laser pulse ionizes the surface layer of the droplet, which expands toward the pulse, and at the same time generates a shock wave that moves to the center of the droplet. From Fig. 10 it is seen that before the arrival of the second pulse, the shock wave does not have time to reach the center of the droplet. Moreover, the penetration depth of the shock wave into the droplet and the thickness of the plasma layer expanding outward are noticeably smaller than the diameter of the laser pulse in the focal spot. In turn, the diameter of the focal spot is noticeably smaller than the diameter of the droplet. In this regard, it is reasonable to assume that the cloud of ionized plasma at the moment of arrival of the second pulse has the form of a short, wide cylindrical channel. We also note that the thickness of the channel is less than the spatial length of the laser pulse, which is $c\tau = 35~\mu$m for a pulse duration $\tau = 120$ fs. With this in mind, we try to simulate the angular distribution of terahertz radiation. By changing the channel length and radius, we try to obtain an angular distribution in the calculations that is in agreement with our experimental data.

To exemplify the spectral and spatial properties of the terahertz radiation from the Sn-In droplet, we consider the current density induced by the laser pulses as a source of terahertz radiation. We introduce the system of coordinates shown in Fig. 5 and make the following assumptions: firstly, the radiating part of the droplet has the shape of a short axially symmetric channel; secondly, the current density is proportional to the electron density (i.e., to the laser intensity), so the vector of the electric current density $\vec{j} = \{j_r, 0, j_z\}$ has the radial and axial components

$$j_r(r,z,t) = -j_0 c\tau \frac{\partial}{\partial z} G, \quad j_z(r,z,t) = j_0 c\tau \frac{1}{r}\frac{\partial}{\partial r} rG, \quad (37)$$

where

$$G = \exp\left[-\frac{r^2}{a^2} - \frac{(z-ct)^2}{c^2\tau^2} - \frac{z^2}{L^2}\right],$$

such that $\text{div}\,\vec{j} = 0$ and $r$ is the radius measured from the optical axis. We used a similar model in our earlier paper [54]. The functions $j_r$ and $j_z$ simulate the spatial distributions of the current density, which serves as a source of terahertz radiation. Both these functions describe a pulse of length $c\tau$, which slowly varies as the pulse propagates in a channel of radius $a$ and length $L$. The specific choice of the function $G$ in the form of the product of Gaussian profiles

as functions of coordinates $r$, $z$, and $t$ does not have a secret meaning and is because it simplifies the subsequent calculation of integrals in an analytic form. As indicated below, by varying the parameters $L$, $a$, and $\tau$, we are able to simulate a qualitative restructuring of the angular distribution of terahertz radiation in a wide range from a narrow beam directed forward to radiation transversely and backward.

The Fourier transform of the vector potential in the wave zone is related to the Fourier transform of the current density [see Eq. (66.7) in Ref. [55]]

$$\vec{j}_{\omega} = \int_{-\infty}^{\infty} dt \, \vec{j}(\vec{x}, t) e^{i\omega t} \qquad (38)$$

through the integral

$$\vec{A}_{\omega}(\vec{R}) = \frac{e^{ikR}}{cR} \int d[3]x' \, \vec{j}_{\omega}(\vec{x}') e^{-ik\vec{n}\cdot\vec{x}'}, \qquad (39)$$

where $\vec{n} = \vec{R}/R = \{\sin(\theta), 0, \cos(\theta)\}$ is the unit vector to the point of observation, and $k = \omega/c$. The magnetic field and the radiated electromagnetic energy are given by

$$\vec{B}_{\omega} = ik(\vec{n} \times \vec{A}_{\omega}), \qquad (40)$$

$$\frac{dW}{do} = R^2 \int_{-\infty}^{\infty} dt \, \frac{B^2}{4\pi} = R^2 \int_{-\infty}^{\infty} \frac{d\omega}{2\pi} \frac{|\vec{B}_{\omega}|^2}{4\pi} \qquad (41)$$

radiated in a given solid angle $do = \sin\theta \, d\theta \, d\phi$. A polar plot of the radiated energy is shown in Fig. 11. The radiated energy is maximum at $\theta = 0$ and approximately 2 times lower at the angle $\theta = 30°$, in accordance with our measurements. We also note that the forward lobe of the angular diagram is very much narrower if $c\tau < (a, L)$. On the other hand, there appears a backward lobe if the channel sizes $a$ and $L$ become too small as compared with $c\tau$. This means that more-accurate measurement of the angular diagram (than is possible in our experiment) could provide more information on the sizes of the channel.

Figure 11 shows the total time-integrated angular distribution obtained for the dimensionless parameters $\tau$, $a$, and $L$ indicated on the caption. Varying these parameters results in quite a wide range of angular patterns, including those with approximately equal forward and backward radiation. Figure 11 shows only one of many patterns, which, in our opinion, most closely fits the experimental measurements.

The rough model that we use to calculate the angular distribution of terahertz radiation does not take into account the presence of the rear edge of the droplet in the path of the laser pulse. Experiments on irradiating a thin foil with a powerful laser show that the thickness of the foil plays a significant role [56]. Schroeder *et al.* [56] attribute the
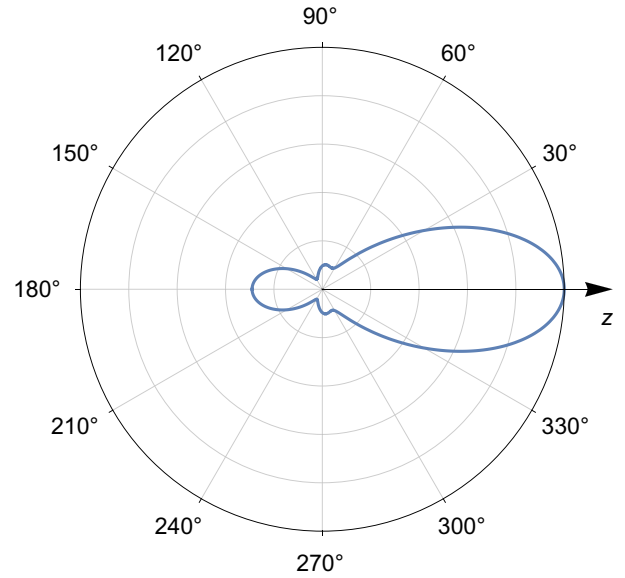


FIG. 11. Angular patterns of $dW/do$ normalized over their maximums for $c\tau = 1$ and $a = L = 0.4$.

radiation through the rear edge of the foil to the effect of the generation of fast electrons by the laser pulse. Crossing the rear boundary of the foil, a bunch of fast electrons with energies from several tens to several hundreds of kiloelectronvolts generates transition radiation.

## V. CONCLUSIONS

In this study we discover a surprising phenomenon: enhanced terahertz radiation from an isolated metal droplet excited by two successive femtosecond laser pulses. As compared with the wavelength range of terahertz radiation, the droplet is a subwavelength source of electromagnetic radiation. The experimental spectrum of terahertz radiation shown in Fig. 8 reaches its maximum at approximately 1 THz, which corresponds to a wavelength of about 300 $\mu$m, whereas the size of the droplet does not exceed about 57 $\mu$m. The radiation we observe has a number of characteristic features. Firstly, the terahertz radiation has a significant forward-directed contribution in relation to the direction of the optical pulse. Secondly, the energy of terahertz radiation depends on the presence of the first laser pulse, which preionizes the droplet before the second-laser-pulse excitation, which generates terahertz radiation. If we optimize the delay between these two pulses, the energy of the terahertz radiation can be increased by 3 orders of magnitude. Thirdly, we demonstrated that the radiation is of coherent origin, as it is well polarized and the polarization state of the terahertz radiation depends on the angle between the directions of oscillations of the electric field vectors in linearly polarized femtosecond pulses, whose directions coincide, and the vertical axis. However, we do not doubt the existence of a small part

of noncoherent thermal radiation. We offer a theoretical model that describes our experimental results.

This model is derived from our previous publications, as well as publications by our colleagues. We assume that, as a result of photoexcitation, additional ionization of the atoms of the metal occurs. The ionization process is described in Sec. IV A. We demonstrate theoretically that the intensity of terahertz radiation is affected by hydrodynamic processes of the movement of ions and free charges in the droplet. The modeling we perform in Sec. IV B confirms the experimental results, which is clearly seen in Figs. 3 and 4. The afore mentioned model shows that the dominating mechanism of generation is the transient photocurrent [1,57]. This transient photocurrent determines the intensity of the terahertz radiation and its spatial distribution. Similarly to what we did to model the process of generation in liquid nitrogen [26], the polarization properties of terahertz radiation in this study can be well described by a phenomenological approach. The interaction of the femtosecond pulse and the droplet of elliptical shape is well depicted by a nonlinear polarization of the second order. The elliptical shape of the droplet is initially discovered with the use of a CCD detector and microscope. Simultaneously, the hypothesis is confirmed by the analysis of the polarization properties of the emitted terahertz radiation.

[1] V. A. Andreeva, O. G. Kosareva, N. A. Panov, D. E. Shipilo, P. M. Solyankin, M. N. Esaulkov, P. González de Alaiza Martínez, A. P. Shkurinov, V. A. Makarov, L. Bergé, and S. L. Chin, Ultrabroad Terahertz Spectrum Generation from an Air-Based Filament Plasma, Phys. Rev. Lett. **116,** 063902 (2016).

[2] L. Bergé, K. Kaltenecker, S. Engelbrecht, A. Nguyen, S. Skupin, L. Merlat, B. Fischer, B. Zhou, I. Thiele, and P. U. Jepsen, Terahertz spectroscopy from air plasmas created by two-color femtosecond laser pulses: The altesse project, Europhys. Lett. **126,** 24001 (2019).

[3] X.-C. Zhang, A. Shkurinov, and Y. Zhang, Extreme terahertz science, Nat. Photonics **11,** 1 (2017).

[4] M. C. Hoffmann, J. Hebling, H. Y. Hwang, K.-L. Yeh, and K. A. Nelson, Impact ionization in insb probed by terahertz pump–terahertz probe spectroscopy, Phys. Rev. B **79,** 161201 (2009).

[5] A. Leitenstorfer, K. A. Nelson, K. Reimann, and K. Tanaka, Focus on nonlinear terahertz studies, New J. Phys. **16,** 045016 (2014).

[6] T. Elsaesser, K. Reimann, and M. Woerner, *Concepts and Applications of Nonlinear Terahertz Spectroscopy*, IOP Concise Physics (Morgan & Claypool Publishers, San Rafael, California,San Rafael, California, 2019).

[7] L. Pálfalvi, J. A. Fülöp, G. Tóth, and J. Hebling, Evanescent-wave proton postaccelerator driven by intense THz pulse, Phys. Rev. ST Accel. Beams **17,** 031301 (2014).

[8] E. A. Nanni, W. R. Huang, K.-H Hong, K. Ravi, A. Fallahi, G. Moriena, R. D. Miller, and F. X. Kärtner, Terahertz-driven linear electron acceleration, Nat. Commun. **6,** 8486 (2015).

[9] K. Y. Kim, J. H. Glownia, A. J. Taylor, and G. Rodriguez, Terahertz emission from ultrafast ionizing air in symmetry-broken laser fields, Opt. Express **15,** 4577 (2007).

[10] Q. Jin, Y. E. K. Williams, J. Dai, and X.-C. Zhang, Observation of broadband terahertz wave generation from liquid water, Appl. Phys. Lett. **111,** 071103 (2017).

[11] T. Ditmire, T. Donnelly, A. Rubenchik, R. Falcone, and M. Perry, Interaction of intense laser pulses with atomic clusters, Phys. Rev. A **53,** 3379 (1996).

[12] C. Wagner and N. Harned, EUV lithography: Lithography gets extreme, Nat. Photonics **4,** 24 (2010).

[13] I. Fomenkov, D. Brandt, A. Ershov, A. Schafgans, Y. Tao, G. Vaschenko, S. Rokitski, M. Kats, M. Vargas, M. Purvis, *et al.*, Light sources for high-volume manufacturing EUV lithography: Technology, performance, and power scaling, Adv. Opt. Technol. **6,** 173 (2017).

[14] R. A. Burdt, Y. Tao, M. S. Tillack, S. Yuspeh, N. M. Shaikh, E. Flaxer, and F. Najmabadi, Laser wavelength effects on the charge state resolved ion energy distributions from laser-produced sn plasma, J. Appl. Phys. **107,** 043303 (2010).

[15] H. Tanaka, A. Matsumoto, K. Akinaga, A. Takahashi, and T. Okada, Comparative study on emission characteristics of extreme ultraviolet radiation from $CO_2$ and Nd : YAG laser-produced tin plasmas, Appl. Phys. Lett. **87,** 041503 (2005).

[16] F. Kadlec, P. Kužel, and J.-L. Coutaz, Optical rectification at metal surfaces, Opt. Lett. **29,** 2674 (2004).

[17] G. Ramanandan, G. Ramakrishnan, N. Kumar, A. Adam, and P. Planken, Emission of terahertz pulses from nanostructured metal surfaces, J. Phys. D: Appl. Phys. **47,** 374003 (2014).

[18] D. K. Polyushkin, I. Márton, P. Rácz, P. Dombi, E. Hendry, and W. L. Barnes, Mechanisms of THz generation from silver nanoparticle and nanohole arrays illuminated by 100 fs pulses of infrared light, Phys. Rev. B **89,** 125426 (2014).

[19] A. V. Balakin, M. S. Dzhidzhoev, V. M. Gordienko, M. N. Esaulkov, I. A. Zhvaniya, K. A. Ivanov, I. A. Kotelnikov, N. A. Kuzechkin, I. A. Ozheredov, V. Y. Panchenko,

A. B. Savel'ev, M. B. Smirnov, P. M. Solyankin, and A. P. Shkurinov, Interaction of high-intensity femtosecond radiation with gas cluster beam: Effect of pulse duration on joint terahertz and X-ray emission, IEEE Trans. Terahertz Sci. Technol. **7,** 70 (2017).

[20] H.-H. Huang, T. Nagashima, W.-H. Hsu, S. Juodkazis, and K. Hatanaka, Dual THz wave and X-ray generation from a water film under femtosecond laser excitation, Nanomaterials **8,** 523 (2018).

[21] Y. Cao, E. Yiwen, P. Huang, and X.-C. Zhang, Broadband terahertz wave emission from liquid metal, Appl. Phys. Lett. **117,** 041107 (2020).

[22] K. Mori, M. Hashida, T. Nagashima, D. Li, K. Teramoto, Y. Nakamiya, S. Inoue, and S. Sakabe, Directional linearly polarized terahertz emission from argon clusters irradiated by noncollinear double-pulse beams, Appl. Phys. Lett. **111,** 241107 (2017).

[23] K. Mori, M. Hashida, T. Nagashima, D. Li, K. Teramoto, Y. Nakamiya, S. Inoue, and S. Sakabe, Increased energy of THz waves from a cluster plasma by optimizing laser pulse duration, AIP Adv. **9,** 015134 (2019).

[24] L.-L. Zhang, W.-M. Wang, T. Wu, R. Zhang, S.-J. Zhang, C.-L. Zhang, Y. Zhang, Z.-M. Sheng, and X.-C. Zhang, Observation of Terahertz Radiation via the Two-Color Laser Scheme with Uncommon Frequency Ratios, Phys. Rev. Lett. **119,** 235001 (2017).

[25] L.-L. Zhang, W.-M. Wang, T. Wu, S.-J. Feng, K. Kang, C.-L. Zhang, Y. Zhang, Y.-T. Li, Z.-M. Sheng, and X.-C. Zhang, Strong Terahertz Radiation from a Liquid-Water Line, Phys. Rev. Appl. **12,** 014005 (2019).

[26] A. V. Balakin, J.-L. Coutaz, V. A. Makarov, I. A. Kotelnikov, Y. Peng, P. M. Solyankin, Y. Zhu, and A. P. Shkurinov, Terahertz wave generation from liquid nitrogen, Photon. Res. **7,** 678 (2019).

[27] V. Savinov, K. Delfanazari, V. A. Fedotov, and N. I. Zheludev, Giant nonlinearity in a superconducting subterahertz metamaterial, Appl. Phys. Lett. **108,** 101107 (2016).

[28] A. Vinokhodov, M. Krivokorytov, Y. Sidelnikov, V. Krivtsun, V. Medvedev, V. Bushuev, K. Koshelev, D. Glushkov, and S. Ellwi, Stable droplet generator for a high brightness laser produced plasma extreme ultraviolet source, Rev. Sci. Instrum. **87,** 103304 (2016).

[29] M. M. Basko, M. S. Krivokorytov, A. Y. Vinokhodov, Y. V. Sidelnikov, V. M. Krivtsun, V. V. Medvedev, D. A. Kim, V. O. Kompanets, A. A. Lash, and K. N. Koshelev, Fragmentation dynamics of liquid–metal droplets under ultra-short laser pulses, Laser Phys. Lett. **14,** 036001 (2017).

[30] A. Y. Vinokhodov, K. N. Koshelev, V. M. Krivtsun, M. S. Krivokorytov, Y. V. Sidelnikov, V. V. Medvedev, V. O. Kompanets, A. A. Melnikov, and S. V. Chekalin, Formation of a fine-dispersed liquid-metal target under the action of femto-and picosecond laser pulses for a laser-plasma radiation source in the extreme ultraviolet range, Quant. Electron. **46,** 23 (2016).

[31] S. A. Akhmanov and R. V. Khohlov, *Problems of Nonlinear Optics* (Gordon and Breach, New York, 1972).

[32] P. D. Cunningham, N. N. Valdes, F. A. Vallejo, L. M. Hayden, B. Polishak, X.-H. Zhou, J. Luo, A. K.-Y. Jen, J. C.

Williams, and R. J. Twieg, Broadband terahertz characterization of the refractive index and absorption of some important polymeric and organic electro-optic materials, J. Appl. Phys. **109,** 043505 (2011).

[33] A. Houard, Y. Liu, B. Prade, V. T. Tikhonchuk, and A. Mysyrowicz, Strong Enhancement of Terahertz Radiation from Laser Filaments in Air by a Static Electric Field, Phys. Rev. Lett. **100,** 255006 (2008).

[34] M. S. Krivokorytov, A. Y. Vinokhodov, Y. V. Sidelnikov, V. M. Krivtsun, V. O. Kompanets, A. A. Lash, K. N. Koshelev, and V. V. Medvedev, Cavitation and spallation in liquid metal droplets produced by subpicosecond pulsed laser radiation, Phys. Rev. E **95,** 031101 (2017).

[35] D. Fisher, M. Fraenkel, Z. Henis, E. Moshe, and S. Eliezer, Interband and intraband (drude) contributions to femtosecond laser absorption in aluminum, Phys. Rev. E **65,** 016409 (2001).

[36] D. F. Price, R. M. More, R. S. Walling, G. Guethlein, R. L. Shepherd, R. E. Stewart, and W. E. White, Absorption of Ultrashort Laser Pulses by Solid Targets Heated Rapidly to Temperatures 1–1000 eV, Phys. Rev. Lett. **75,** 252 (1995).

[37] *Tablitzy Fizicheskikh Velichin*, edited by I. K. Kikoin (Atomizdat, Moscow, 1976) (in Russian).

[38] L. D. Landau and E. M. Lifshitz, in *Quantum Mechanics*, Course of Theoretical Physics, Vol. III (Pergamon, New York, 1991), third edition, revised and enlarged ed.

[39] S. J. J. Thomson, XLII. ionization by moving electrified particles, Phil. Mag. Ser. 6 **23,** 449 (1912).

[40] *Lectures on Plasma Physics*, edited by I. A. Kotelnikov (Binom, Moscow, 2013) (in Russian).

[41] I. A. Kotelnikov and A. I. Milstein, Electron radiative recombination with a hydrogen-like ion, Phys. Scr. **94,** 055403 (2019).

[42] M. M. Murnane, H. C. Kapteyn, M. D. Rosen, and R. W. Falcone, Ultrafast X-ray pulses from laser-produced plasmas, Science **251,** 531 (1991).

[43] A. Sasaki, A. Sunahara, H. Furukawa, K. Nishihara, S. Fujioka, T. Nishikawa, F. Koike, H. Ohashi, and H. Tanuma, Modeling of radiative properties of sn plasmas for extreme-ultraviolet source, J. Appl. Phys. **107,** 113303 (2010).

[44] N. R. Laboratory, *NRL Plasma Formulary* (Naval Research Laboratory, Washington, 2016).

[45] The difference between $\tau_{ei}$ and $\tau_{ie}$ is explained in many textbooks on plasma physics; see, for example, Ref. [40]. The electron-ion collision time characterizes the rate of electron scattering on ions, which leads to the transformation of the directed average velocity of electrons to their chaotic (thermal) velocity. The ion-electron collision time characterizes the rate of energy exchange between electrons and ions, which is suppressed because of huge difference between their masses.

[46] Ya. B. Zel'dovich and Yu. P. Raiser, *Physics of Shock Waves and High-Temperature Hydrodynamic Phenomena* (Academic Press, New York, 1966).

[47] A. Kemp and J. M. ter Vehn, An equation of state code for hot dense matter, based on the QEOS description, Nucl. Instrum. Methods Phys. Res. Sect., A: Accel. Spectrom. Detect. Assoc. Equip. **415,** 674 (1998).

[48] S. Faik, A. Tauschwitz, and I. Iosilevskiy, The equation of state package FEOS for high energy density matter, Comput. Phys. Commun. **227**, 117 (2018).

[49] S. I. Braginsky, in *Reviews in Plasma Physics* (Gosatomizdat, Moscow, 1983), Vol. 1, p. 193.

[50] M. M. Basko, Ralef-2d: Excerpts from the main report (KIAM, Moscow, 2017).

[51] L. Spitzer, *Physics of Fully Ionized Gases* (Courier Corporation, New York, 2006).

[52] A. F. Nikiforov, V. G. Novikov, and V. B. Uvarov, *Quantum-Statistical Models of Hot Dense Matter. Methods for Computation Opacity and Equation of State* (Birkhäuser, Switzerland, 2005), p. 428.

[53] M. Born and E. Wolf, *Principles of Optics* (Pergamon, Oxford, 1980), 6th ed.

[54] A. P. Shkurinov, A. S. Sinko, P. M. Solyankin, A. V. Borodin, M. N. Esaulkov, V. V. Annenkov, I. A. Kotelnikov, I. V. Timofeev, and X.-C. Zhang, Impact of the dipole contribution on the terahertz emission of air-based plasma induced by tightly focused femtosecond laser pulses, Phys. Rev. E **95**, 043209 (2017).

[55] L. D. Landau and E. M. Lifshitz, in *The Classical Theory Fields*, Course of Theoretical Physics, Vol. II (Butterworth & Heinemann, New York, 1998), 4th ed.

[56] C. B. Schroeder, E. Esarey, J. van Tilborg, and W. P. Leemans, Theory of coherent transition radiation generated at a plasma-vacuum interface, Phys. Rev. E **69**, 016501 (2004).

[57] A. V. Borodin, M. N. Esaulkov, I. I. Kuritsyn, I. A. Kotelnikov, and A. P. Shkurinov, On the role of photoionization in generation of terahertz radiation in the plasma of optical breakdown, J. Opt. Soc. Am. B **29**, 1911 (2012).

[58] https://refractiveindex.info